Weather and Climate Extremes 34 (2021) 100368

Contents lists available at ScienceDirect

Weather and Climate Extremes

journal homepage: www.elsevier.com/locate/wace

Simulating the storm environment responsible for Nepal's first observed tornado

Jonathan David Douglas Meyer [a,b,*], Binod Pokharel [a,b,c], Robert R. Gillies [a,b]

[a] Department of Plants, Soils, and Climate, Utah State University, Logan, UT, USA
[b] Utah Climate Center, Utah State University, Logan, UT, USA
[c] Central Department of Hydrology and Meteorology, Tribhuvan University, Kathmandu, Nepal

ARTICLE INFO

Keywords:
Tornado
Nepal
WRF Model

ABSTRACT

A high-resolution numerical forecast model was used to simulate the meteorological conditions leading up to the March 31st, 2019 severe weather event that produced Nepal's first-ever observed tornado. The sparse meteorologic observations in the region capturing the storm environment limit the ability to anticipate another similar situation should the particular set of conditions present themselves again. This study presents a multifaced view of the storm environment through 1) a synoptic perspective provided by the Global Data Assimilation System (GDAS) reanalysis dataset and 2) a trio of progressively higher resolution one-way nested simulations (12 km–4km–1km) driven by GDAS boundary conditions to more closely examine the storm-scale environment. GDAS data and numerical simulations revealed moderately strong instability throughout the region with CAPE values between 1000 and 2000 J kg^{-1} K^{-1} and lifted index values between −4 and −7. Vertical wind profiles featuring little directional shear and moderate velocity shear yielded shear-based convective indices that suggested slight potential for rotating supercell thunderstorms. Within this environment, the 1-km simulation produced strong, rotating convection in nearly the same location and at nearly the same time as the observed tornadic storm. Lastly, an assessment of the limited number of observed historical tornadic events in the region showed that with amply convective available potential energy, the 2019 Nepal tornado environment stood out for the limited vertical directional wind shear present.

1. Introduction and background

On March 31st, 2019, an extreme and unprecedented convective scenario unfolded in the Bara and Parsa districts of south-central Nepal where thunderstorms brought strong winds and hail to the mostly rural landscape. While severe weather in this region is not itself unprecedented (Nepal specifically experiences elevated rates of thunderstorms and windstorms during the pre-monsoon months of March–May; Aryal, 2018; Mäkelä et al., 2014), the March 31st event was headlined by the country's first-ever recorded tornado; resulting in 30 fatalities, 1150 injuries, and 2890 families becoming homeless (Report on Bara Parsa Tornado, 2019; hereafter referred to as BPT Report). Fig. 1a shows some of the damage a rural community sustained from the storm.

Although this is the country's first-observed tornado, the lower elevation Indian-Bangladesh region to the southeast of Nepal has experienced infrequent tornadic storms. Historical accounts starting 1835 studied by Peterson and Mehta (1981) documented 51 possible tornadoes across Bengal, 18 of which killed 10 people or more, while Goldar et al. (2001) documented 36 possible spring tornadoes between 1890 and 2000 over West Bengal, 14 of which killed 10 people or more. Rosoff and Hindman (2002) studied the deadly severe weather outbreak, which brought deadly tornadoes to the region and severe non-tornadic storms throughout Nepal including a well-documented Mt. Everest storm that took the lives of eight climbers. Unfortunately, Nepal (and the surrounding region in general) has a limited observational network; Nepal specifically lacks weather RADAR coverage and has only a single upper-air sounding. To better study the underlying storm environment, more recent tornadic events in the region over the last few decades have been studied through high-resolution numerical modeling (Litta et al., 2010; Litta et al., 2012; Das et al., 2015). Bikos et al. (2016) conducted high-resolution numerical simulations of ten high-impact tornadic events in Bangladesh and found that similar to U.S. tornadic storms, Bangladesh storms were characterized by relatively high instability and sufficient deep-layer vertical wind shear.

* Corresponding author. Department of Plants, Soils, and Climate, Utah State University, Logan, UT, USA.
E-mail address: jon.meyer@usu.edu (J.D.D. Meyer).

https://doi.org/10.1016/j.wace.2021.100368
Received 27 January 2021; Received in revised form 13 May 2021; Accepted 5 August 2021
Available online 12 August 2021

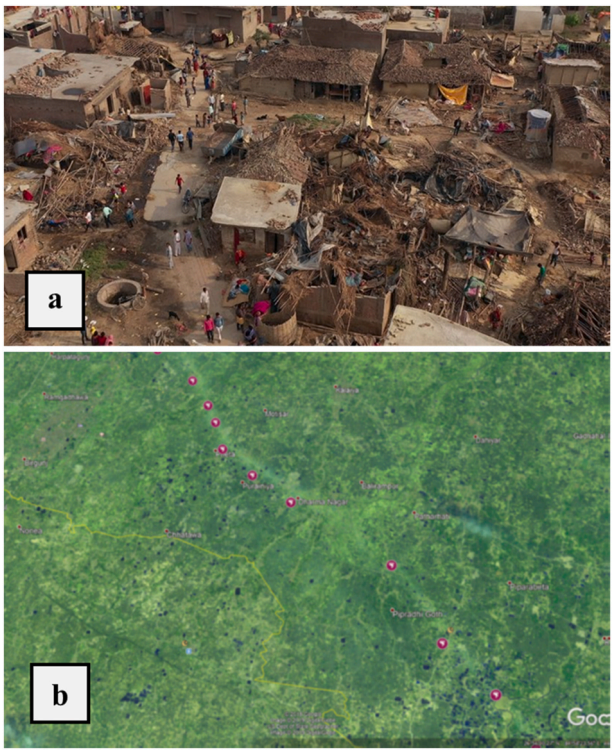

Fig. 1. (a) damage photo from a rural village in Nepal taken from Khatri (2019) and (b) reproduction of the visible satellite image and damage path from Fig. 1.2 of the Bara-Parsa Tornado Report.

In the wake of the March 2019 storm, the region's limited observation and instrumentation infrastructure initially clouded the ability of meteorologists to comprehensively evaluate the event. At the time of the event, Nepal had no Doppler radar coverage; however, the country has since installed a lone weather radar site in Western Nepal. In addition to a sparse network of surface observing stations, the country's sole rawinsonde vertical profiling site located in the central Nepal capital city of Kathmandu did capture a 00 UTC morning sounding, but the afternoon 12 UTC sounding was not measured. Outside of satellite remote sensing and the limited ground-based observations, very little meteorological information was available to investigate the background storm environment or the storms themselves. In fact, it was not until the April 5th damage survey and concurrent personal witness interviews outlined in the BPT report before the question of whether the event's damaging winds were tornadic or straight-line in nature was conclusively addressed.

Initial satellite imagery and ground-based surveys revealed a 90-km-long damage path (Mallapaty, 2019) with a width that ranged from 200 m to 750 m (BPT report, 2019). Fig. 1b shows a visible satellite image of the storm damage path. The collection of witness reports and CCTV timestamps suggested an average propagation speed of the tornado of approximately 34 km/h (BPT report, 2019). Structural damage indicators based on the Enhanced Fujita Scale (WSEC, 2004) estimated wind speeds between 180 km/h (112 mph) and 265 km/h (165 mph), which is equivalent to an EF2-EF3 tornado.

With ample ground-based evidence outlined in the BPT report, little doubt is left that the March 31st event was indeed the first recorded tornado in Nepal's history. Understandably, the Nepalese government dedicated a section of the BPT report to outlining planned improvements to forecaster training and situational awareness to better anticipate such conditions should they develop again. However, the lack of knowledge on the pre-storm environment or the storm morphology drives a need to ascertain more information on atmospheric conditions; specifically, the thermodynamic and vertical wind shear profiles and any mesoscale interactions with the region's complex terrain. Adding to this body of regional modeling examination of severe storm environments, this study uses a high-resolution numerical model to simulate Nepal's storm environment to better understand the conditions present.

Through an evaluation of coarse global reanalysis data, this study compliments the large-scale atmospheric conditions outlined in the BPT report. The bigger question pertaining to the previously unresolved small-scale conditions leading up to the storm, and whether these ingredients were supportive of supercell thunderstorms were addressed with a high-resolution, convective resolving numerical model. The purpose of this study and the numerical simulation is to document with finer detail the storm environment and resulting convective storm morphology. Through this level of scrutiny, it is also our hope to supplement the BPT report's goals of guiding forecaster training and operational situational awareness.

A discussion of the data used to assess the meteorological conditions as well as those used to drive the numerical model are provided in

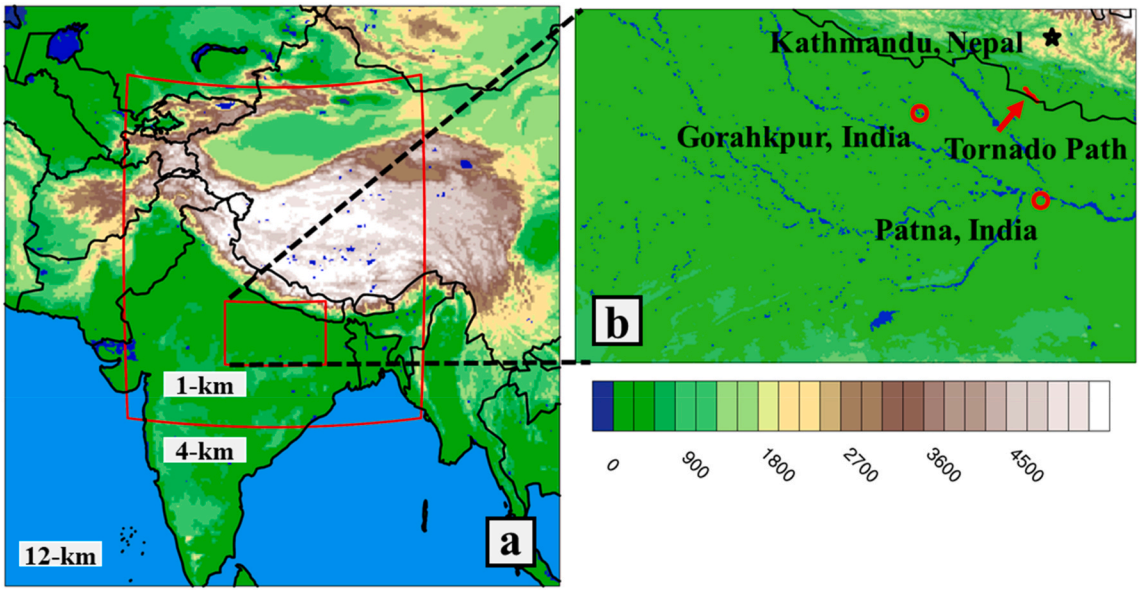

Fig. 2. WRF one-way nested model domains with the model-resolved topography included. Domain grid spacing is 12-km, 4-km, and 1-km, respectively.

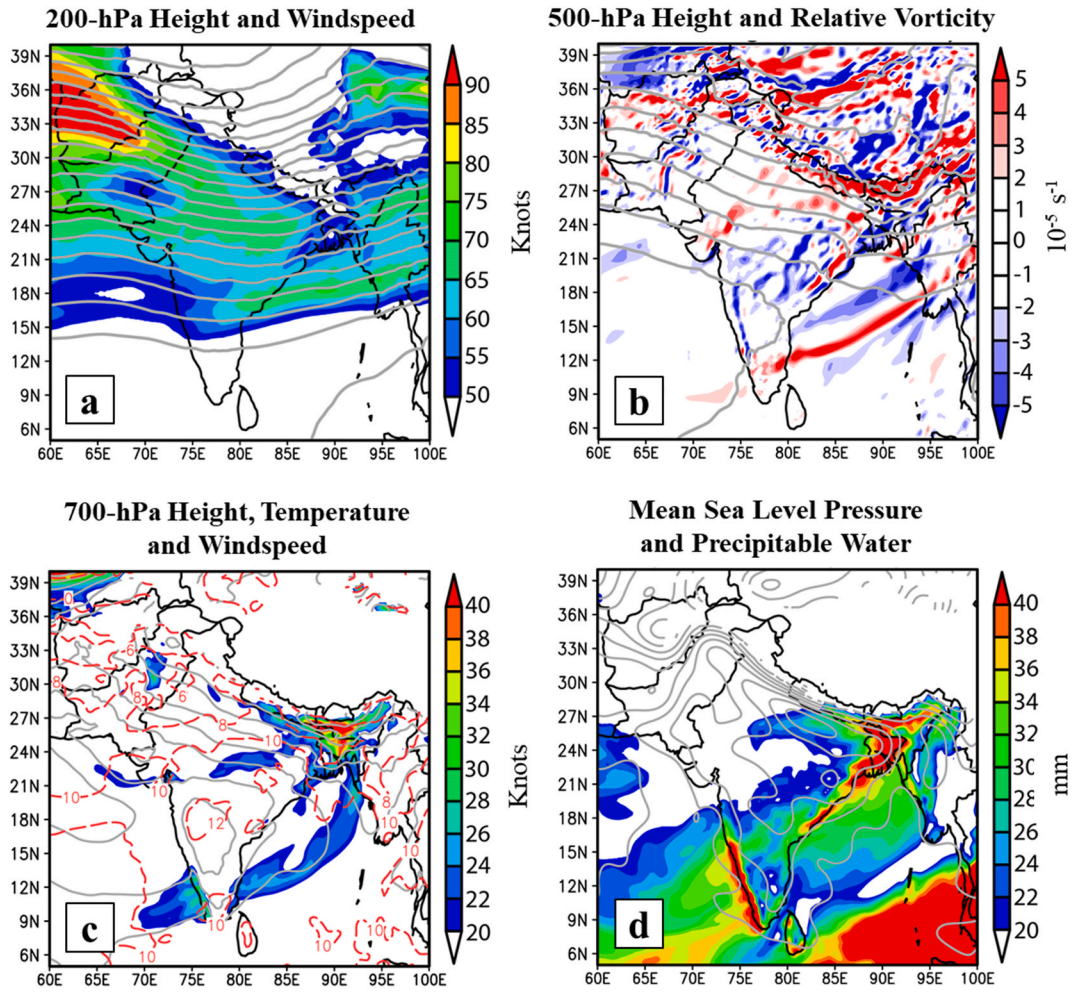

Fig. 3. 12:00 UTC 31st March (a) 200-hPa winds (knots; color fill) and geopotential height (m; contours); (b) 500-hPa vorticity (10^{-5} s^{-1}; color fill) and geopotential height (m; contours); 700-hPa temperature (°F; dashed red lines), geopotential height (m; contours) and wind speed (knots; color fill); (d) MSLP (hPa; contour), Pwat (mm; color fill). (For interpretation of the references to color in this figure legend, the reader is referred to the Web version of this article.)

Section 2 while the model configuration is provided in Section 3. An overview of the synoptic pre-storm environment including the thermodynamic conditions is discussed in Section 4. Analysis of the simulated storm environment is provided in Section 5 with an examination of the storm morphology presented in Section 6. A comparison of the 2019 Nepal conditions with past tornadic events in the surrounding region is presented in Section 7 before the final discussion and concluding remarks provided in Section 8.

2. Data

This section will provide a brief overview of the available meteorological observations pertinent to the discussions and analysis presented within this paper. For a more exhaustive overview of the available observations, we direct the reader to the BPT report.

2.1. Global data assimilating system

The Global Data Assimilation System (GDAS) is an observation assimilation platform developed by the National Center for Environmental Prediction (NCEP) to blend surface observations, balloon data, wind profiler data, aircraft reports, buoy observations, radar observations, and satellite observations onto a 0.25° by 0.25° 3-dimensional grid. For this study, GDAS data acted as the initial and lateral boundary conditions for the numerical simulations and also provided context for the meteorological conditions on that day. Because of the lack of first-order observations in Nepal, a great deal of dynamical interpolation goes into describing the region's conditions.

2.2. Upper air soundings

Upper-air balloon (rawinsonde) soundings provide valuable insight into the storm-defining thermodynamic and vertical wind shear environment. Unfortunately, throughout all of Nepal, only a single rawinsonde profile at the capital city of Kathmandu is measured. In fact, the region in general suffers from a limited network of rawinsonde measurements with the closest soundings launched in the northern Indian cities of Gorahkpur and Patna (Fig. 2b). A further limitation to diagnosing the vertical structure of the atmosphere is that while the common practice in upper-air networks dictates twice-daily measurements (~00 UTC and 12 UTC), the region's trio of soundings are only measured once per day at ~00 UTC. The timing of these balloon releases falls more than 12 h before the severe weather event developed as well as before daytime heating modifies the boundary layer.

3. Model configuration

Given the lack of meteorologic observations and the extensive extrapolation of Nepal's conditions within global reanalysis products, numerical modeling is necessary to describe in sufficient detail the highly nuanced meteorological conditions over Nepal. This study employs the Weather Research and Forecasting (WRF) model (Skamarock

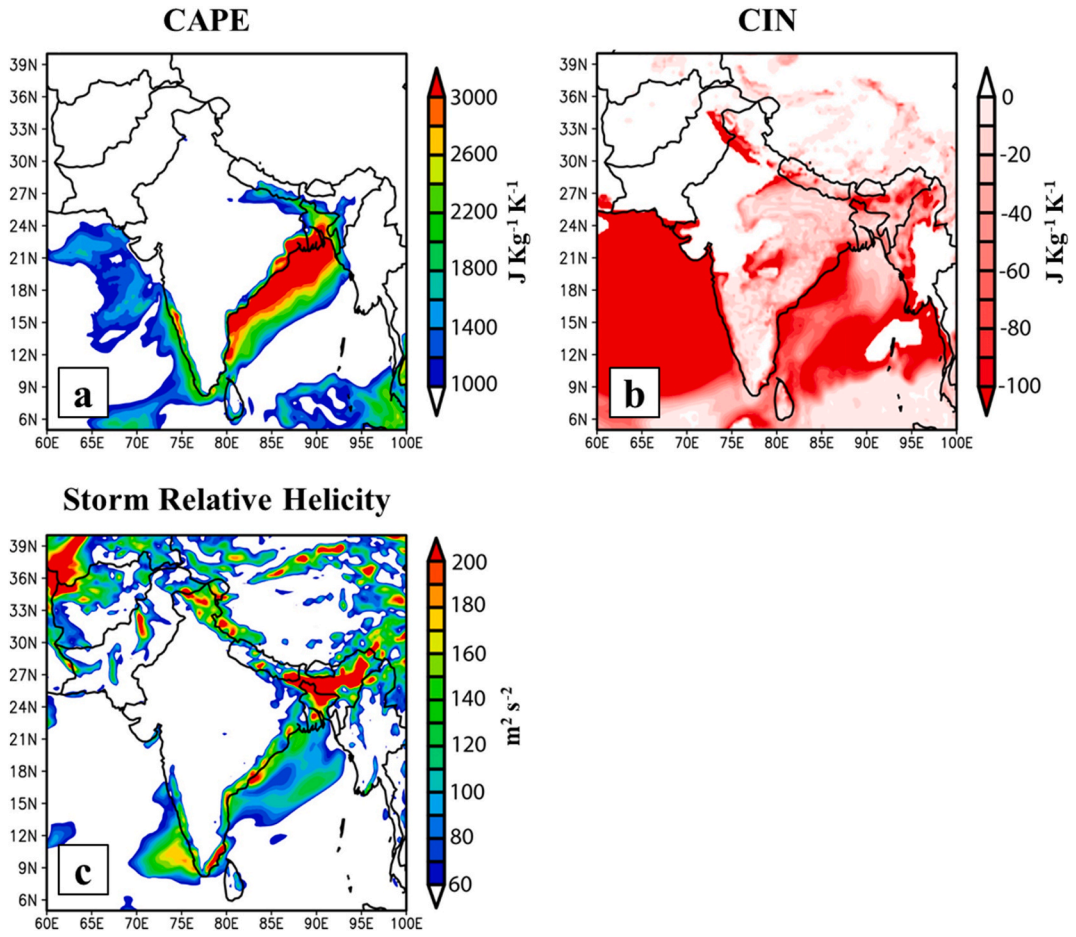

Fig. 4. 12:00 UTC convective indices captured by GDAS data with (a) Convective Available Potential Energy (CAPE; J Kg^{-1} K^{-1}), (b) Convective Inhibition (CIN; J Kg^{-1} K^{-1}), and (c) Storm Relative Helicity (m^2 s^{-2}).

et al., 2008) to dynamically downscale the GDAS forcing data. WRF's ability to customize the domain and model physics is ideal to simulate the unique nature of the convective environment and the region's complex terrain. To capture the full diurnal evolution of the storm environment, 24-h WRF simulations were initialized 18 UTC March 30th, 2019 and completed 18 UTC, March 31st.

3.1. Domain design

To properly downscale the GDAS data, this study used a trio of domain's nested within each other to gradually scale down to the necessary convective-resolving resolutions. Fig. 2 illustrates the placement of these three domains, which employ one-way nesting to scale from 12-km, 4-km, and 1-km grid spacing, respectively. Also indicated in Fig. 2b is the path of the observed tornado (red line) and three surrounding cities where upper-air rawinsondes are deployed.

Given the weak synoptic forcing on this day and the complex terrain in the immediate vicinity, one-way nesting was chosen based on findings by Soriano et al.,(2004) that showed one-way nesting can outperform two-way nesting under these conditions. 52 vertical layers were used for all domains. The outermost domain is driven with the six-hourly GDAS data. Three-hourly output from domain 1 is used to drive the 4-km domain 2, where 30-min output is in-turn used to drive the innermost 1-km domain. 15-minute output from the 1-km domain provides a useful assessment of the evolution of the storm environment.

3.2. Model physics

Model physics employed by this study are consistent across all three domains with the exception of the Kain Fritsch cumulus parameterization (Kain, 2004), which is turned off in the convective permitting 4-km and 1-km domains. With a focus that this study should help inform the Nepalese forecasting community, many of the model physics options here follow what is operationally run by the North American Mesoscale (NAM) model, which shares the same underlying dynamics engine as WRF. WRF Microphysics employed the WSM 6-class graupel scheme (Hong and Lim, 2006), Mellor–Yamada Nakanishi Niino (MYNN) Level 2.5 scheme (Nakanishi and Niino, 2009) for planetary boundary layer, RRTMG radiation schemes for both longwave and shortwave (Iacono et al., 2008), the Unified Noah Land Surface Model (Tewari et al., 2004) and the Eta Similarity Scheme (Janjic, 1994) for the surface layer physics.

4. GDAS pre-storm environment

The large-scale atmospheric conditions preceding the convective event are first explored with the coarse-resolution GDAS data. This analysis serves to 1) document the large-scale background conditions present for the convective event and 2) provide background context for the subsequent exploration of the simulated environment provided by the high-resolution WRF domains discussed in Section 5.

Fig. 3 shows the upper-air conditions for 12:00 UTC, March 31st (just before the severe weather outbreak) An upper-level shortwave trough is located immediately upstream of Nepal (Fig. 3a). While the strongest jet

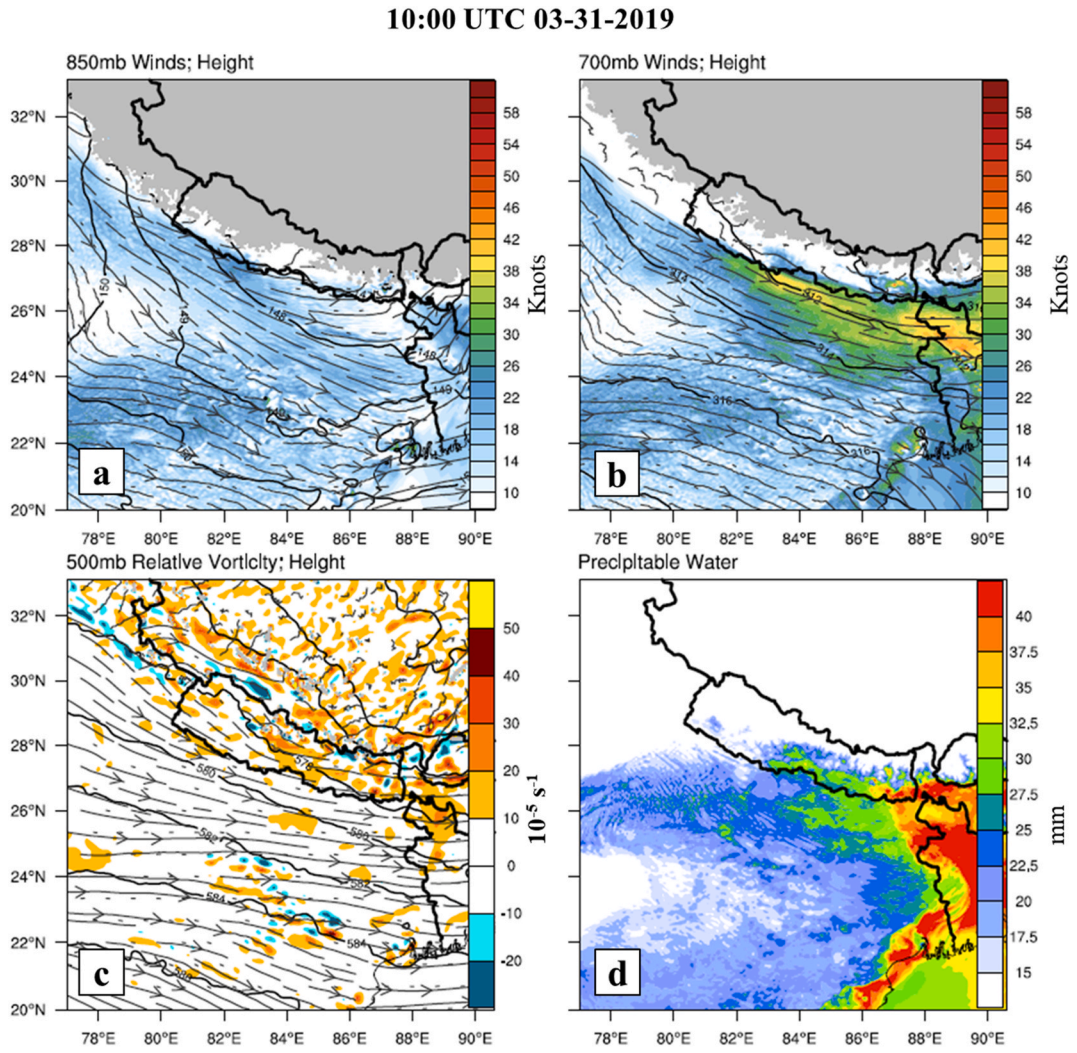

Fig. 5. Model simulated surface and upper-air conditions from the intermediate 4 km domain of (a) 850-hPa winds (knots; color fill), streamlines and geopotential height (meters; contours), (b) 700-hPa streamlines and geopotential height (meters; contours), (c) 500-hPa relative vorticity (10^{-5} s^{-1}; color fill) and geopotential height (meters; contour), and (d) precipitable water (mm; color fill). (For interpretation of the references to color in this figure legend, the reader is referred to the Web version of this article.)

stream winds are associated with a super-geostrophic jet streak rotating over Iran and Afghanistan, weaker jet stream winds generally less than 70 ms^{-1} are found over Nepal. Mid-level analysis at 500-hPa (Fig. 2b) indicates the shortwave trough has shifted downstream of Nepal, although cyclonic vorticity is still advecting over Nepal ahead of a smaller shortwave propagating through the upstream side of the main shortwave trough. The advection of this cyclonic vorticity serves as a potential convective trigger mechanism given the right underlying static stability. At 700-hPa (Fig. 3c), a prevailing northwesterly wind field is directed perpendicular to the terrain gradient, which contributes to the presence of regional cyclonic curvature. Given the indicated temperature gradient, the orientation of the 700-hPa wind field and the presence of a low-level jet is likely associated with a thermal wind enhancement to the synoptic circulation. The horizontal shear associated with the region's terrain and thermal wind could play a role in the generation of helicity and reinforce rotating updrafts in a storm. At the surface (Fig. 3d), a low-pressure center is found to the southwest of Nepal and is driving a weak southeasterly circulation that in additional to insinuating low-level directional wind shear, is also acting to draw a tongue of elevated precipitable water (Pwat) into the Nepal lowlands.

Fig. 4 shows a collection of convective indices for the 12:00 UTC, March 31st GDAS data. Convective Available Potential Energy (CAPE; Fig. 4a) describes the measure of tropospheric instability, with CAPE values of <1000 J kg^{-1} considered weak instability, 1000–2500 J kg^{-1} considered moderate instability, and >2500 J kg^{-1} considered strong instability. The Nepalese region exhibits moderate instability with CAPE values between 1000 J kg^{-1} and 2000 J kg^{-1}. Convective Inhibition (CIN; Fig. 4b) describes the measure of thermodynamic resistance that an air parcel must overcome before the parcel can take advantage of the profile's CAPE. Over the region of interest, GDAS data shows a modest convective cap with CIN values between 20 J kg^{-1} and 100 J kg^{-1}. Assessing the wind shear over the lower 3 km of the atmosphere, Storm Relative Helicity (SRH; Davies-Jones et al. (1990)) provides a general assessment of the atmosphere's potential for cyclonic updraft rotation in right-moving supercells. Generally, SRH values greater than 100 m^{-2} s^{-2}, like those found in the region of interest, are considered favorable for tornadic storms; we note, however, that there are no clear boundaries of SRH between tornadic and non-tornadic storms.

Overall, favorable large-scale fluid dynamics and vertical thermodynamic ingredients were found leading up to the convective event. The elevated humidity and temperature profile created a thermodynamically unstable situation with high CAPE and low CIN values while low-level wind shear indicated helicity was co-located with the convective environment. In addition to the buoyant atmosphere, the presence of mid-

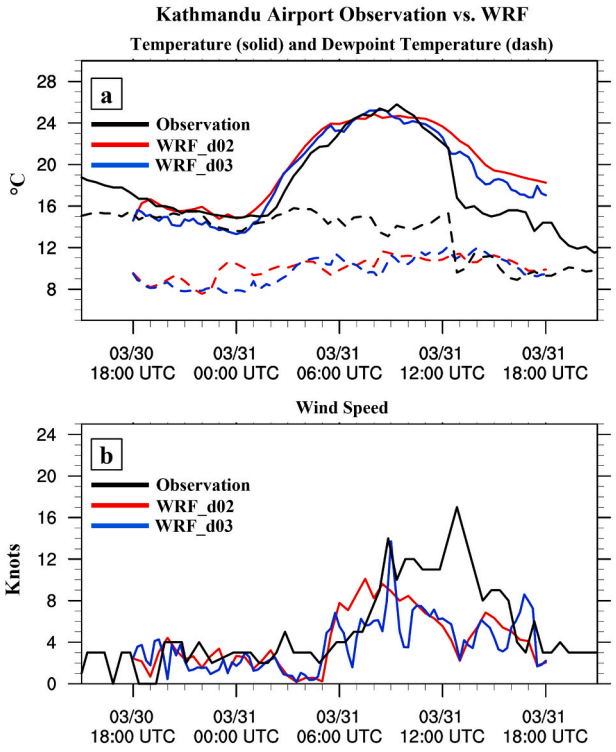

Fig. 6. Comparison of surface weather station observations from the Kathmandu Airport (black) and the nearest WRF model gridpoint from domain 2 (red) and domain 3 (blue). Temperature (°C; solid line) and dewpoint temperature (°C; dashed line) are shown in (a) with wind speed (knots) shown in (b). (For interpretation of the references to color in this figure legend, the reader is referred to the Web version of this article.)

level cyclonic vorticity advection and an upstream upper-level shortwave trough translating overhead also provided convective trigger mechanisms in the Nepal region.

5. WRF model simulations

This section presents an analysis of the mesoscale environment simulated by the WRF model when driven by the aforementioned large-scale GDAS conditions. To address what mesoscale conditions were likely present for the event, the 4-km domain is evaluated as it provides a sufficiently high-resolution representation of the regional Nepal storm environment. The higher resolution 1-km domain provides enough fidelity to address questions surrounding basic storm type and morphology that develops as a result of the convective environment. While the observed storms occurred roughly 13–14 UTC (7–8pm LST), the subsequent analysis assesses the pre-storm afternoon environment by focusing on roughly the peak daytime heating conditions at 10 UTC (4pm LST) March 31st.

5.1. Pre-storm mesoscale environment

We begin by assessing the near-surface to mid-level atmosphere to examine the state of the boundary layer winds and thermodynamic properties immediately before convective triggering. Fig. 5 shows the presence of the low-level jet at 700-hPa (Fig. 5b) oriented parallel to the Himalayan terrain with the northernmost edge of the jet overlying the India-Nepal border. The core of this low-level jet exhibits speeds approaching 40 knots along with slight cyclonic curvature. Just as was shown in the GDAS data (Fig. 3) a mid-level shortwave disturbance is present in the WRF simulations (Fig. 5c). As a result, modest positive vorticity advection is translating through central Nepal. Underneath the shortwave, elevated Pwat values on the order of 20–30 mm are found throughout the southern and central Nepalese lowlands; spatial and magnitude values of this moisture plume agree with the GDAS data.

5.2. Pre-storm thermodynamic environment

To evaluate the WRF model's ability to reproduce observed conditions, Fig. 6 provides a timeseries of the simulated conditions versus the surface weather observations nearest to the observed storm. Observations recorded at the Tribhuvan International Airport located in Kathmandu, Nepal (black lines; geographic location indicated in Fig. 2b) are compared with the nearest WRF model gridpoint from both the intermediate 4-km domain (red lines) and the innermost 1-km domain (blue lines). We note that Kathmandu is nearly 100-km away from the path of the observed tornado, so observed storm conditions at the Tribhuvan International Airport are not expected to be associated with the supercell thunderstorm that spawned the severe weather. With that, comparing the observations of temperature and dewpoint temperature in Fig. 6a validates the model's ability to closely match the pre-storm temperature environment while exhibiting a dry dewpoint temperature bias of ~3–5 °C. Coincident with the development of the observed tornadic storm impacting to the south and west of Kathmandu, a rapid drop in temperature and dewpoint temperature at around 12:30 UTC indicates the passage of a storm's surface cold pool. Observed increasing wind speeds (knots) between 06:00 UTC and 12:00 UTC shown in Fig. 6b were also well captured by the WRF model domains, however the model does not reflect the peak gusts observed from 09:00 UTC to 13:00 UTC. A more co-located comparison with the impacted Bara-Parsa region would be preferable to test the skill of the WRF model, however, no such observations were available at the time of this study.

For the Patna and Gorakhpur, India and Kathmandu, Nepal locations (Fig. 2b), Fig. 7 compares observed 00 UTC March 31st rawinsonde soundings (solid lines) of temperature (black), dewpoint temperature (blue), and wind barbs with the 4 km domain's simulated profiles (dashed lines) from the nearest model gridpoint. Positive CAPE trajectories were computed based on the most unstable air parcel and are plotted in red (no red line indicates the profile has no CAPE). Additionally, wind hodographs are presented in the upper right corner of each Skew-T to compare the vertical profile of wind shear.

Outside of near-surface conditions, modeled atmospheric profiles strongly agree with the observed rawinsonde profiles. 00 UTC is ~ 6am LST, so each of the three locations exhibit a well-developed nocturnal surface temperature inversion along with a fairly humid profile of dewpoints temperatures. Greatest discrepancies between the modeled and observed profiles are found right at the surface, where the modeled profiles exhibited cold and dry biases at each location. While the modeled temperature profiles quickly converge towards the observed profile above the surface, low-level humidity remains slightly dry-biased through the low- and middle-levels for the higher elevation Kathmandu location (corroborating the dry biases found in the surface station comparison [Fig. 6]). The lower elevation Patna and Gorakhpur soundings exhibit a slightly elevated dewpoint profile above ~700-hPa.

Despite a fairly similar overall profile of environmental temperature and dewpoint temperature, the sensitivity of an air parcel's adiabatic trajectory to surface conditions where the cold and dry modeled biases (specifically the dry bias) results in modeled CAPE values that appears to be much less convectively favorable. Herein lies one significant disadvantage of there being no 12 UTC sounding as we are unable to evaluate model biases in buoyancy during daytime heating when the surface boundary layer has been turbulently mixed. However, given the consistency between observed and modeled profiles immediately above the surface, we are confident that the modeled buoyancy leading up to the event would be more comparable to the actual atmosphere than the nocturnal CAPE values would indicate. A fourth Skew-T is shown in Fig. 7d, which represents a 10 UTC pre-storm WRF simulated profile simulated near the observed storm track. Positive CAPE of nearly 2000 J

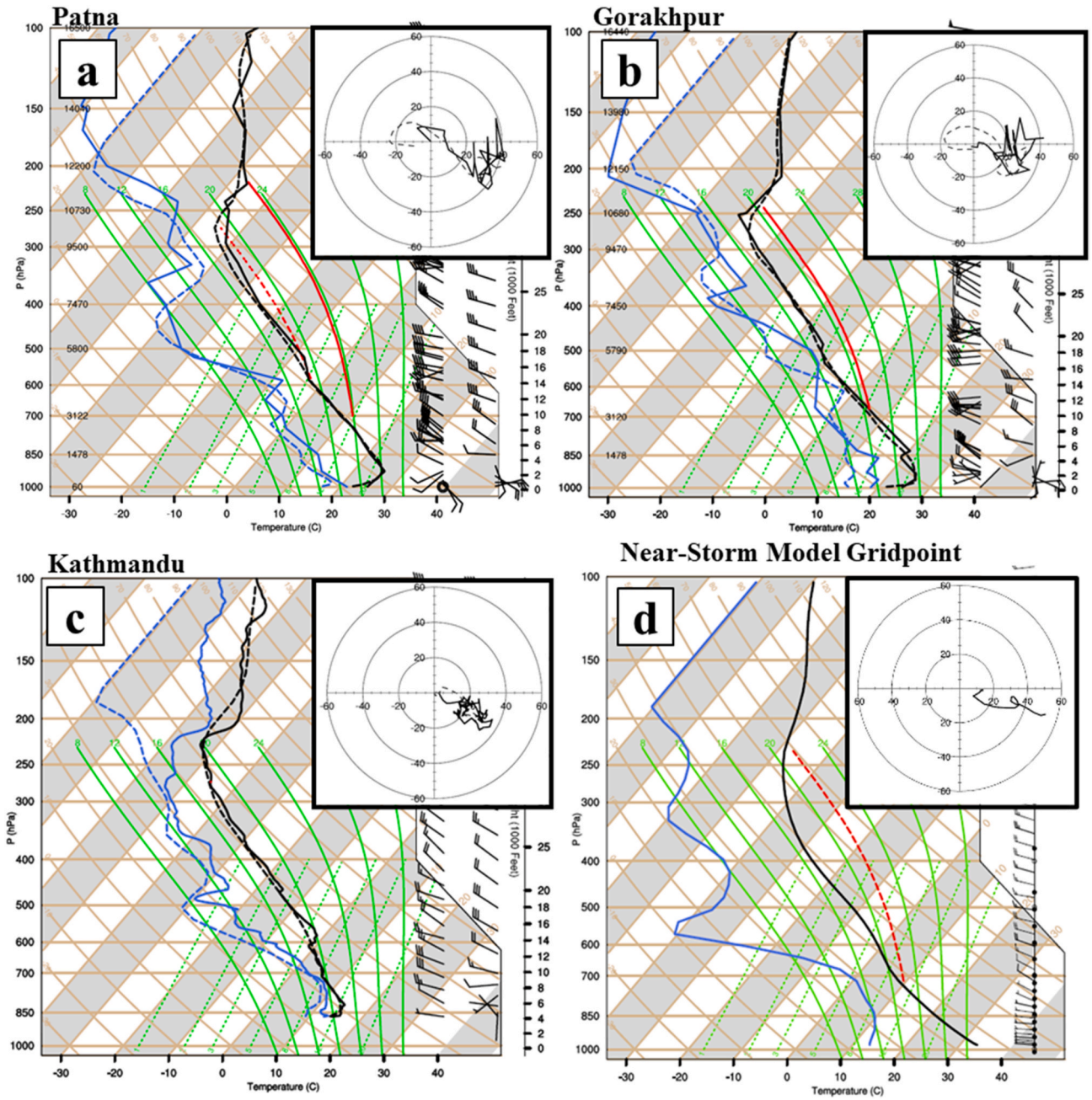

Fig. 7. Comparison between 00:00 UTC March 31st rawinsonde observations (solid lines) of temperature (black) and dewpoint temperature (blue) and the nearest simulated WRF gridpoint (dashed lines) for (a) Patna, India, (b) Gorakhpur, India, and (c) Kathmandu, Nepal balloon sites. A hodograph is included in the upper right corner which illustrates the vertical profile of the observations (solid) and WRF (dashed) wind speed and directions. A fourth Skew-T (d) shows the WRF simulated pre-storm environment (10:00 UTC) near the observed storm track. The positive CAPE trajectory is noted with the dashed red line. (For interpretation of the references to color in this figure legend, the reader is referred to the Web version of this article.)

kg^{-1} K^{-1} was simulated and is shown with the red dashed line.

Regarding the vertical wind profile, the state of directional and velocity shear is critical in the evaluation of the atmosphere's proclivity towards tornadic thunderstorms. We note that each of the profiles are dominated by mostly northwesterly velocity shear with a small degree of near-surface directional shear present in the observed profiles and lesser so in modeled profiles (increasingly so by the 10 UTC profile (Fig. 7d). Again, the greatest model discrepancies are found under the nocturnal surface inversion which experience significant modification during daytime heating as evidenced by the nearly dry adiabatic lapse rate within the simulated surface convectively mixed layer shown in Fig. 7d.

5.3. Simulated convective indices

Convective indices are commonly referenced in operational forecasting as they provide an expedited assessment of the potential convective storm types the environment of buoyancy and vertical wind shear could support. Storm type thresholds are rough approximations based on empirical relationships with observed storms outcomes and it is important to note that, as pointed out by Doswell and Schultz (2006), the use of many diagnostic convective indices in operational forecasting may or may not be suitable or representative of physical processes and as such, may provide little value in predicting realized storm types (e.g. Monteverdi et al., 2003). Given Nepal's unique terrain and high surface

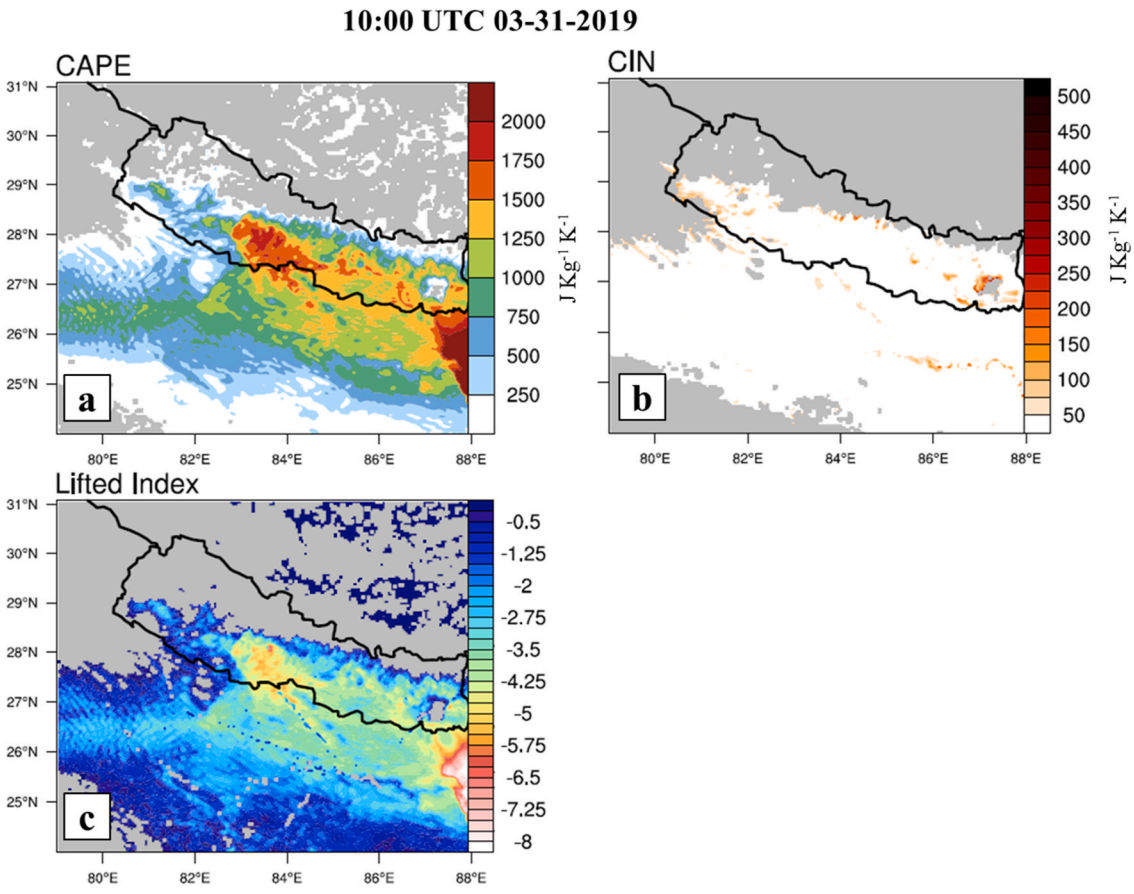

Fig. 8. 10:00 UTC model-simulated convective indices of a) Convective Available Potential Energy (CAPE; J Kg^{-1} K^{-1}), b) Convective Inhibition (CIN; J Kg^{-1} K^{-1}, and c) Lifted Index.

elevation, this caveat is especially relevant when referencing convective indices to diagnose potential storm types. However, for the purpose of this study, the comparative baseline provided by convective indices affords a sufficient approach to address the questions of 1) what degree of static stability was present, 2) what was the nature of the vertical directional and velocity wind shear profiles, and 3) was the collective buoyancy and shear environment favorable or unfavorable of supercell thunderstorms?

Our assessment of these questions begins with Fig. 8, which compares the 10 UTC (4pm LST) buoyancy-based indices of CAPE, CIN, and Lifted Index (LI; Galway, 1956). LI values describes the degree of mid-level instability by comparing the environmental temperature at 500-hPa with the temperature an air parcel (in our case a mixed layer averaged over the lowest 1-km) adiabatically lifted to 500-hPa would have. Lifted indices of −1 to −4 are generally indicative of marginal instability, −5 to −7 for large instability and < −8 considered extreme instability. Moderate instability is shown over central Nepal with CAPE values of ~1000–2000 J kg^{-1} K^{-1} and LI values ranging between −3 and −6. While CIN values earlier in the day suggests a capping inversion was present (not shown), by the later afternoon 10 UTC hour, little to no CIN is present meaning there would be little convective resistance should a convective trigger occur.

To assess the degree of wind shear, Fig. 9 presents simulated SRH, the Energy-Helicity index (EHI; Davies, 1993), the Bulk Richardson Number shear term (BRS; Weisman and Klemp, 1982; Droegemeier et al., 1993), and the Supercell Convective Parameter (SCP; Thompson et al., 2003). With the exception of a local pocket in central Nepal, pre-storm shear parameters are not meaningfully large regarding supercell favorability. However, a region of more favorably large shear parameters is found just south of Nepal; collocated with the presence of the low-level jet core (Fig. 5b). While the optimal shear characteristics are not found where the observed tornado occurred, SRH values in central Nepal were found to peak around 150 m^2 s^{-2}, which falls on the lower end of favorable values for tornadic storms.

EHI is designed to capture the observed relationship between high CAPE and SRH values during tornadic storms. Again, while no specific boundary exists for delineating tornadic vs. non-tornadic storms, just like SRH values, central Nepal's ~1–1.5 EHI values are interpreted to indicate the buoyancy and shear terms are weakly balanced and favorable for weak tornadic storms. Much like EHI, the Bulk Richardson number (BRN) is a dimensionless ratio assessing buoyancy and shear. The denominator of the BRN equation shown in Fig. 9c represents the speed shear between the surface wind and the 0–6 km layer mean wind. Because the point of this parameter is to diagnose the differential vertical torquing forces applied to a storm's updraft by wind shear, the wind profile over such a deep layer is typically first weighted based on a column-normalized air density profile before the mean layer wind speed is calculated; doing so better captures the differential profile of momentum an updraft is subjected to. BRS values above 35–40 m^2 s^{-2} have been associated with tornadic storms (Stensrud et al., 1997) and central Nepal exhibits values approaching the lower range of supercell favorability. We note that if density weighting is not applied to the wind profile, a much greater amount of BRS well into the range of expected supercells was present in central Nepal.

Finally, the SCP parameter (Fig. 9d) distills multiple convective indices to attempt to quantify the co-location of both tornadically-favorable CAPE, SRH, and BRS regions. Each parameter is normalized to supercell "threshold" values. Empirical studies show that SCP values above ~2 are sufficient for weak tornadic storms. In the Nepal region, small pre-storm SCP values were simulated. SCP values tend to be on the

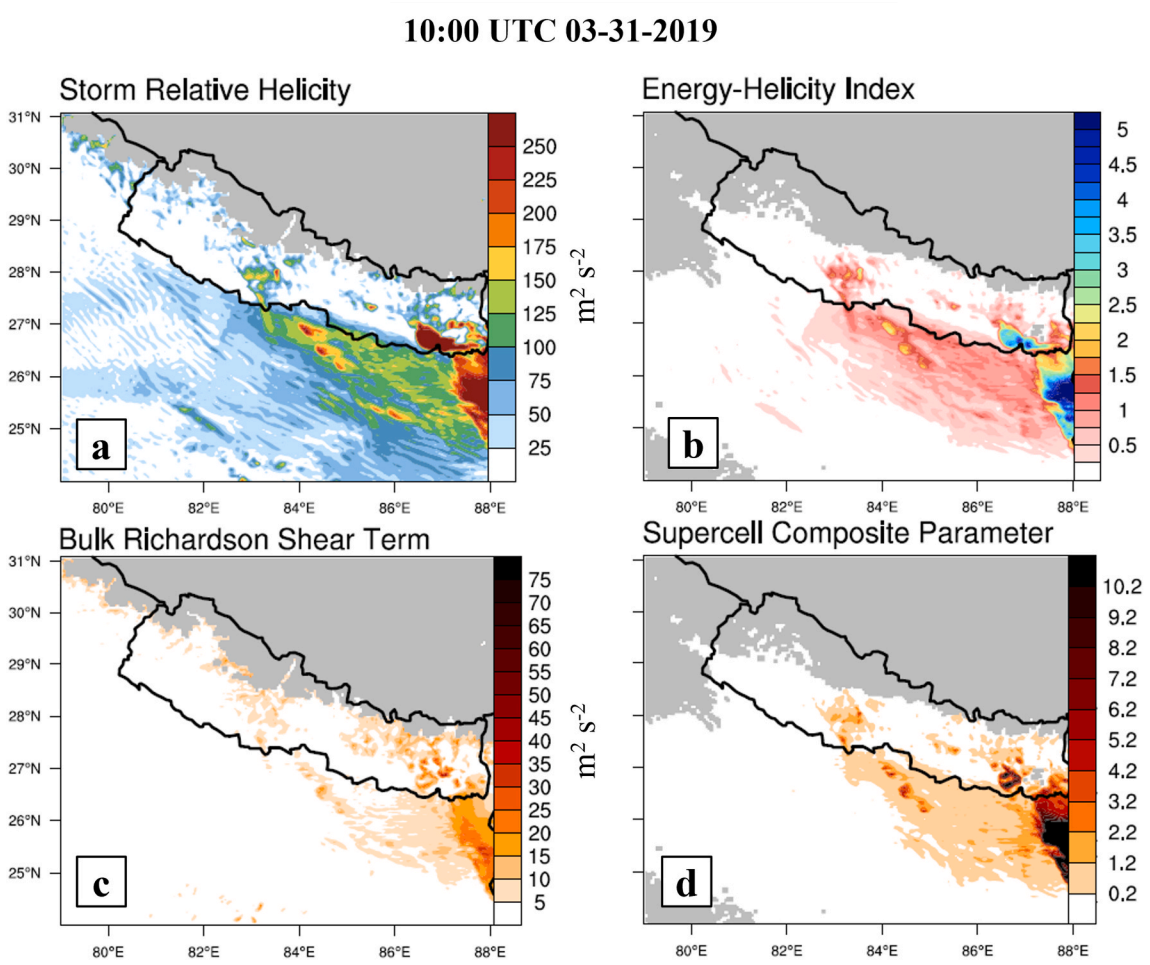

Fig. 9. Same as Fig. 8, but for shear-based convective indices of a) Storm Relative Helicity (SRH; $m^2\ s^{-2}$), b) Energy Helicity Index (EHI), c) Bulk Richardson Number shear term ($m^2\ s^{-2}$) and d) Supercell Composite Parameter (SCP).

low side of supercell favorability at best, likely a result of the limited shear. We note that convective activity associated with the severe weather outbreak does exist with much higher SCP and shear values as the near-storm wind field contains much greater low-level shear (not shown).

Collectively, the buoyancy-based convective indices (CAPE, CIN, LI) portray a pre-storm environment supportive of strong convection while the wind profile and the shear-based SRH index portrays an environment dominated by moderate velocity shear compared to limited near-surface directional shear. Despite the limited directional shear, composite indices such as EHI and SCP the co-location of instability and wind shear together weakly favors rotating thunderstorms.

6. Simulated storm analysis

Given the unstable nature of the atmosphere, scattered, multicellular convection was present over the Himalayan foothills throughout the daytime (not shown). Storm motions throughout the day follow the mean-layer wind vector oriented roughly east-southeasterly. The scattered convection dissipated during the midafternoon hours; replaced by an isolated, more intense thunderstorm that triggered over the lip of the Himalayan terrain. Simulated maximum "composite" radar reflectivity (dBZ) provided in Fig. 10 shows the evolution and movement of the strong, isolated thunderstorm through the innermost (1 km) WRF domain. Compared with the earlier multicell convection, Fig. 10's storm motions exhibit a more south-easterly storm motion as the storm propagated down over the central Nepal lowlands. The deviation from previous convection and the departure from the mean layer wind vector, the south-southeasterly storm motions of Fig. 10's storm are more characteristic of a right-moving supercell (Bunkers et al., 2000). The storm maintained peak intensity for roughly an hour between 12 UTC and 13 UTC with maximum reflectivity values greater than 50 dBZ associated with the storm's updraft. The storm sustained intense reflectivity values before dissipating between 13:45 UTC and 14:00 UTC. Compared to the observed storm track and timing, the simulated storm's lifecycle is remarkably similar. Observations in the BPT Report suggest the tornado occurred during the late stage of the storm's life cycle, so while the peak intensity of the simulated storm occurred approximately an hour before the observed event, the simulated storm was still substantial during the tornadic 13:00–14:00 UTC window. While the storm track's most intense duration was located roughly 50 miles upstream of the observed event, the storm motions are comparable between the observed and the simulated storm as well as the damage path.

To address the question of whether the simulated convection exhibited rotation and was capable of producing a tornado, Fig. 11 shows the 1-km innermost domain's simulated 500-hPa vertical velocity (solid and dashed contour lines; $m\ s^{-1}$) and updraft helicity (color filled contours; $m^2\ s^{-2}$). Updraft helicity describes the measure of rotation in storm updrafts by integrating the product of the updraft velocity and the vertical component of vorticity over the 2-km to 5-km layer; with values typically ranging between 25 and 250 $m^2\ s^{-2}$ for tornadic storms (Kain et al., 2008). Storm updrafts and downdrafts are delineated with solid and dashed contours lines, respectively. From the storm's early stages,

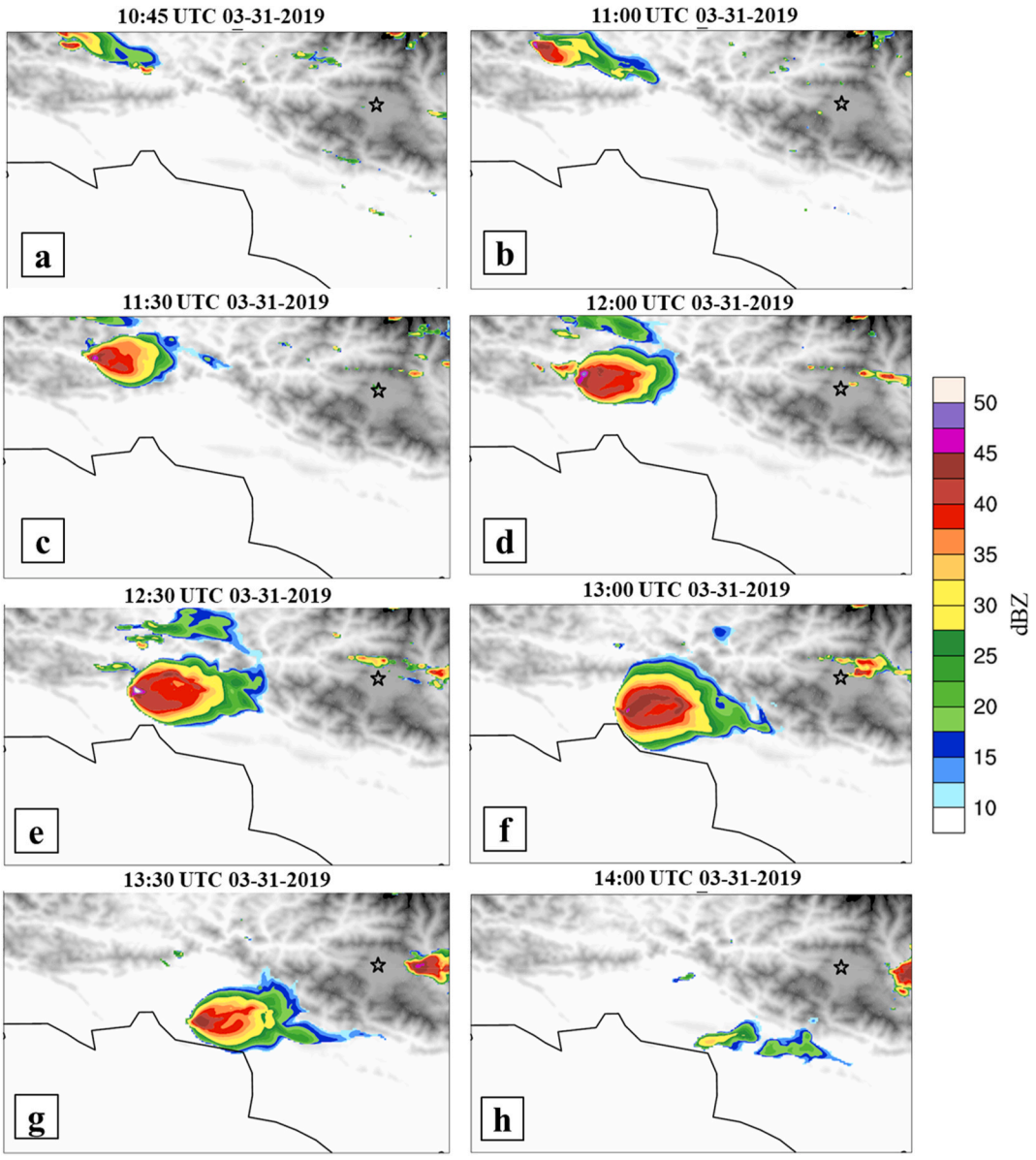

Fig. 10. Model simulated max composite reflectivity (dBZ) from the innermost 1-km WRF domain. Terrain is provided with gray shading, while Kathmandu, Nepal is indicated with the star marker for reference.

mesocyclone rotation in the isolated updraft is apparent while a forward flank downdraft forms and matures between 11:00 and 11:30 UTC. A strong inflow notch for the updraft is also present during the early stages. Hints of a minor 500-mb rear-flank downdraft (RFD) are shown between 12:00 UTC and 13:00 UTC with a more apparent RFD captured in 700-mb vertical motions on the order of 2 m s^{-1} (not shown) by 13:00 UTC. Between 11:30 UTC and 12:30 UTC the storm structure begins to evolve and exhibit the morphology of a mature supercell thunderstorm (Klemp et al., 1981; Moller et al., 1994; Davies-Jones et al., 2001). By 1300 UTC, the storm's updraft and downdraft structure is that of a prototypical supercell thunderstorm with a "v-notch" structure to the forward flank downdraft and a hook-echo appearance to vertical velocity analogous to that commonly found in supercell radar signatures. Between 13:30 UTC and 13:45 UTC, the simulated storm's helicity began to dissipate with the updraft entirely dissipated by 13:45 UTC.

7. Historical comparison with past tornadic events

This section serves to briefly compare the 2019 tornadic storm environment with the region's most recent tornadic storms over the past thirty years (Litta et al., 2010; Litta et al., 2012; Das et al., 2015). Fig. 12 presents wind vectors from ERA-5 reanalysis (Hersbach et al., 2020) for three previous documented tornadic storms in the region for April 09, 1993 (a), March 24, 1998 (b), March 31, 2009 (c) and the March 31, 2019 Nepal case (d). The 925-hPa (blue), 700-hPa (red) and 500-hPa (green) wind vectors approximate the nature of each event's low and mid-level wind shear profiles. In addition to the more inland geographical position and higher elevation, what sets the 2019 case apart from these past events is the lack of low-level directional wind shear. While we have shown the 2019 event occurred under a more uni-directional wind profile (Fig. 7), Fig. 12 highlights the more significant near-surface directional wind shear in each of the past events. In each past event, southerly to southwesterly low-level winds existed underneath westerly mid-level winds. The veering wind profile is more typical for an environment supportive of supercell thunderstorms making the lack of such a profile in the 2019 Nepal event more unique.

We also note that each of the three previous cases are located coincidental with an onshore flow of a humid maritime air mass. While the

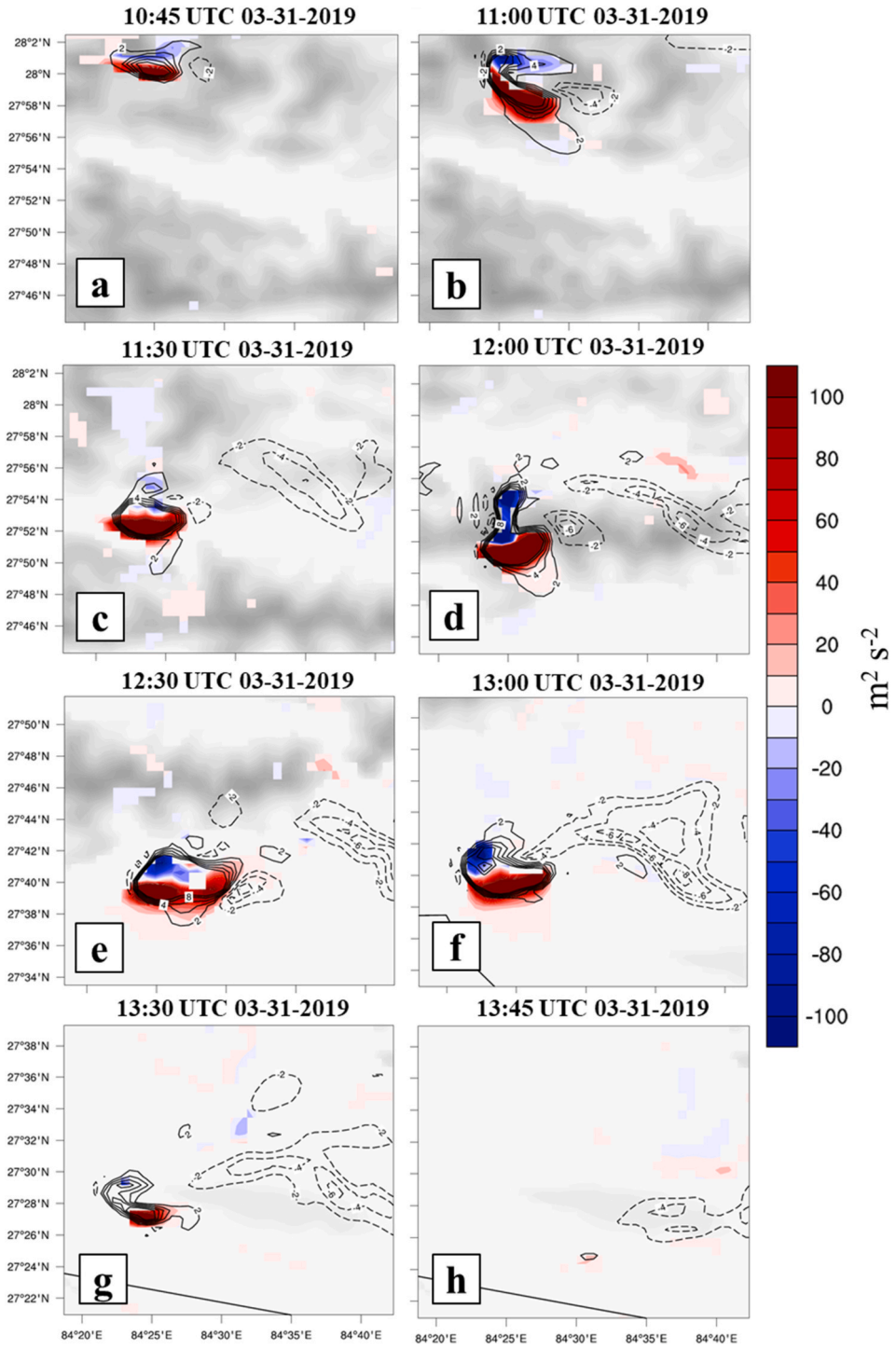

Fig. 11. 1-km innermost model domain simulated updraft helicity (color fill; $m^2\ s^{-2}$), vertical velocity (contour lines; $m\ s^{-1}$) and topography (gray shading). Storm updrafts and downdrafts are shown with solid and dashed contour lines, respectively. (For interpretation of the references to color in this figure legend, the reader is referred to the Web version of this article.)

2019 Nepal event's environment did have a strong low-level jet advancing into Bangladesh similar to the past events, the environment over south-central Nepal was far removed from this feature and would not be impacted by the source of high low-level humidity and directional wind shear.

While any tornadic event will feature a background environment with elevated thermodynamic instability (i.e., high CAPE), the comparison presented here shows just how unique 2019 Nepal event's wind profile was in contrast with the region's historical tornadic outbreaks but also in contrast of general tornadic storm environments where low-level shear is considered as one of the most important ingredients for an environment to produce rotating supercell thunderstorms.

8. Discussion and conclusion

To understand the undocumented small-scale conditions leading up to Nepal's first-observed tornadic event, this study employed a high-resolution, convective-resolving numerical model to ask the question

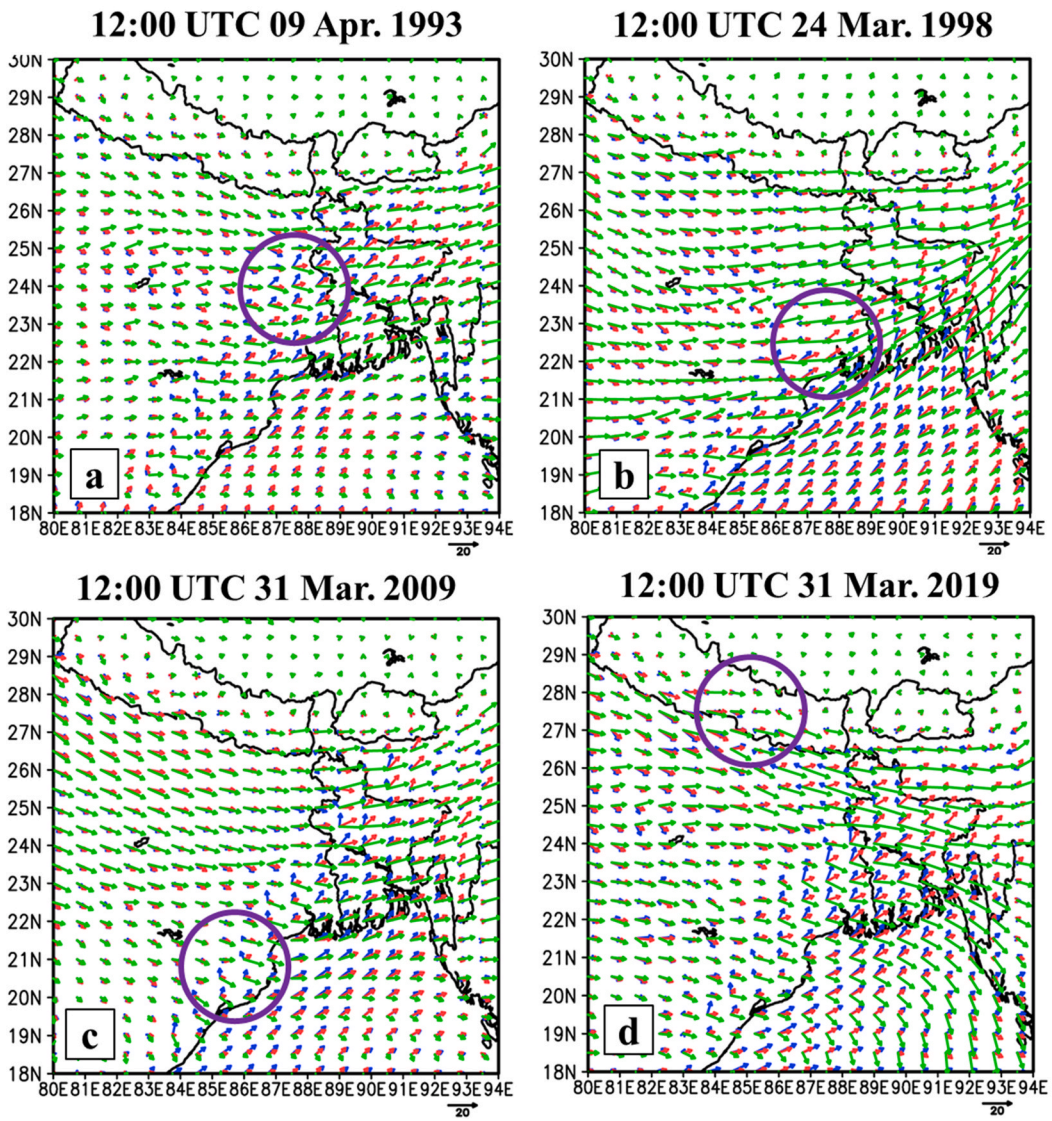

Fig. 12. Comparison of ERA-5 wind vectors at 925-hPa (blue), 700-hPa (red) and 500-hPa (green) for three historical cases and the 2019 Nepal tornado event. Purple circles represent the approximate region where the tornadic activity was observed. (For interpretation of the references to color in this figure legend, the reader is referred to the Web version of this article.)

of 1) what were the mesoscale meteorological conditions leading up to the severe weather and 2) were those conditions favorable for a tornadic supercell? The purpose of this study was not only to document the storm environment at resolutions beyond coarse-resolution gridded reanalysis datasets, but to question whether a supercell storm could be simulated under these conditions. In that, we hope to serve future operational forecaster's anticipation of such an extreme severe weather scenario.

The synopsis of atmospheric conditions showed both a convectively favorable atmosphere and one that featured sufficient convective trigger mechanisms. Buoyancy- and shear-based convective indices presented evidence for weak to moderate supercell conditions although we reiterate that convective indices and storm-type thresholds are empirical in nature, are not quantitative, and are not grounded in a specific physical mechanism. As such, the use of convective indices and stated storm-type thresholds documented in the literature to diagnose potential storm types in such a meteorologically-nuanced region like Nepal should be considered relative with malleable thresholds for expected storm types.

The accuracy of the storm timing and location with respect to observations lend credibility that the simulated environment match that of the actual storm environment. Updraft helicity and vertical velocity of the simulated storm showed a strongly rotating updraft and an updraft/downdraft structure resembling a classic supercell thunderstorm suggesting that the environment was indeed capable of producing supercell thunderstorms. Given convective indices indicated the potential for strong convection alongside shear-based metrics showing weak favorability for supercell thunderstorms suggests that such extreme severe weather, while rare, have the potential to be anticipated in the future. While additionally operational tools and training are being implemented by Nepal's Department of Hydrology and Meteorology (DHM, BPT report), the success of this study to simulate the severe weather event highlights the benefit of a regional, high-resolution operational forecasting model. We emphasize that operational modeling domains are typically far more computationally constrained than numerical case studies such as what was presented here. While 1-km high-resolution domains such as the one used for this study's innermost domain are unrealistic for operational purposes, we have shown that the more operationally feasible 4-km domain is capable of simulating the ingredients necessary to anticipate severe convective environments. Such resolution domains (or better) are already in operational use at continental scales (e.g. National Center for Environmental Prediction's 3-km High-Resolution Rapid Refresh [Benjamin et al., 2016] and North American Mesoscale-3km domains [NAM technical report, 2017]).

In the wake of this study, future work cataloging the climatology of similar storm environments (whether tornado reports occurred or not) would be useful to provide historical context for just how unique this specific event was and to frame the scenarios leading to the type of storm environments that have produced the rare tornadic events. We have shown that the 2019 Nepal tornado occurred under less-than-typical directional wind shear when compared to the collection of recent regional tornadic events. How rare such a convective and wind profile environment would be contextually useful when developing future forecasting training. Furthermore, numerical downscaling of a collection of these historic events would provide additional context on how likely (or unlikely) these convective situations are to produce supercell thunderstorms. While outside of the scope of this study's purpose, the storm's lifecycle which began over the Himalayan highlands before descending down the foothills and out over the Nepalese lowlands does present a unique situation for an even higher resolution numerical study to address the question of whether the local-scale terrain interactions influenced the storm dynamics in a way that enhanced the environmental conditions and ultimately led to tornadogenesis.

Author statement

Jonathan Meyer: Modeling, Methodology, Analysis, Writing- Original draft preparation and revision process. Binod Pokharel: Methodology, Analysis, Observational Data Acquisition Writing- Reviewing and Editing. Robert Gillies: Writing- Reviewing and Editing.

Declaration of competing interest

The authors declare that they have no known competing financial interests or personal relationships that could have appeared to influence the work reported in this paper.

Acknowledgements

The authors wish to acknowledge the Utah Agricultural Experiment Station support under grant number #9509. The authors also wish to acknowledge contributions made during the analysis and manuscript preparation by Dr. Shih-Yu (Simon) Wang of Utah State University's Dept. of Plants, Soils, and Climate. We acknowledge and appreciate the observation datasets provided by Barun Paudel from the Department of Hydrology and Meteorology in Nepal. We also thank the valuable contributions made by the anonymous reviewers and the journal editor.

References

Aryal, D., 2018. Pre-monsoon thunderstorm in Nepal. Int. J. Rural Dev. Environ. Health Res. 2 (3), 39–45. https://doi.org/10.22161/ijreh.2.3.5.

Benjamin, S.G., et al., 2016. A North American hourly assimilation and model forecast cycle: the Rapid Refresh. Mon. Weather Rev. 144, 1669–1694. https://doi.org/10.1175/MWR-D-15-0242.1.

Bikos, D., Finch, J., Case, J.L., 2016. The environment associated with significant tornadoes in Bangladesh. Atmos. Res. 167, 183–195.

Bunkers, M.J., Klimowski, B.A., Zeitler, J.W., Thompson, R.L., Weisman, M.L., 2000. Predicting supercell motion using a new hodograph technique. Weather Forecast. 15, 61–79.

Das, M.K., Das, S., Chowdhury, M.A.M., Karmakar, S., 2015. Simulation of tornado over Brahmanbaria on 22 March 2013 using Doppler weather radar and WRF model. Geomatics, Natural Hazards and Risk 7 (5), 1–23. https://doi.org/10.1080/19475705.2015.1115432.

Davies, J.M., 1993. Hourly helicity, instability, and EHI in forecasting supercell tornadoes. In: Preprints, 17th Conf. On Severe Local Storms. Amer. Meteor. Soc., St. Louis, MO, pp. 107–111.

Davies-Jones, R.P., Burgess, D.W., Foster, M., 1990. Test of helicity as a tornado forecast parameter. In: Preprints, 16th Conf. On severe local storms, Kananaskis Park, AB, Canada. Amer. Meteor. Soc., pp. 588–592

Davies-Jones, R., Trapp, R.J., Bluestein, H.B., 2001. Tornadoes and tornadic storms. In: Doswell, C.A. (Ed.), Severe Convective Storms. Meteorological Monographs. American Meteorological Society, Boston, MA. https://doi.org/10.1007/978-1-935704-06-5_5.

Doswell III, C.A., Schultz, D.M., 2006. On the use of indices and parameters in forecasting severe storms. Electron. J. Severe Storms Meteor. 1 (3), 1–22.

Droegemeier, K.K., Lazarus, S.M., Davies-Jones, R., 1993. The influence of helicity on numerically simulated convective storms. Mon. Weather Rev. 121 (7), 2005–2029.

Galway, J.G., 1956. The lifted index as a predictor of latent instability. Bull. Am. Meteorol. Soc. 43, 528–529.

Goldar, R.N., Banerjee, S.K., Debnath, G.C., 2001. Tornado in India and neighborhood and its predictability. Regional Met. Centre, Alipore, Kolkata. Issued by Office of the Additional Director General of Meteorology (Research), Meteorological Office of India Meteorological Department, Pune, India.

Hersbach, H., Bell, B., Berrisford, P., Co-authors, 2020. The ERA5 global reanalysis. Q. J. R. Meteorol. Soc. 146, 1999–2049. https://doi.org/10.1002/qj.3803.

Hong, S.-Y., Lim, J.-O.J., 2006. The WRF single–moment 6–class microphysics scheme (WSM6). J. Kor. Meteor. Soc. 42, 129–151.

Iacono, M.J., Delamere, J.S., Mlawer, E.J., Shephard, M.W., Clough, S.A., Collins, W.D., 2008. Radiative forcing by long–lived greenhouse gases: calculations with the AER radiative transfer models. J. Geophys. Res. 113, D13103. https://doi.org/10.1029/2008JD009944.

Janjic, Z.I., 1994. The step-mountain Eta coordinate model: Further developments of the convection, viscous layer, and turbulence closure schemes. Monthly Weather Review 122, 927–945. https://doi.org/10.1175/1520-0493(1994)122<0927:TSMECM>2.0.CO;2.

Kain, J.S., 2004. The Kain–Fritsch Convective Parameterization: An Update. Journal of Applied Meteorology 43 (1), 170–181. https://doi.org/10.1175/1520-0450(2004)043<0170:TKCPAU>2.0.CO;2.

Kain, J.S., Weiss, S.J., Bright, D.R., Baldwin, M.E., Levit, J.J., Carbin, G.W., Schwartz, C. S., Weisman, M.L., Droegemeier, K.K., Weber, D.B., Thomas, K.W., 2008. Some practical considerations regarding horizontal resolution in the first generation of operational convection-allowing NWP. Weather Forecast. 23 (5), 931–952.

Khatri, P.P., 2019. Had Tornado Hit Bara-Parsa, Southern Nepal? Meteorologists Are Not Sure. https://nepal24hours.com/had-tornado-hit-bara-parsa-southern-nepal- meteorologists-are-not-sure/. (Accessed 26 January 2021).

Klemp, J.B., Wilhelmson, R.B., Ray, P.S., 1981. Observed and numerically simulated structure of a mature supercell thunderstorm. J. Atmos. Sci. 38 (8), 1558–1580.

Litta, A.J., Mohanty, U.C., Bhan, S.C., 2010. Numerical simulation of a tornado over Ludhiana (India) using WRF-NMM model. Meteorol. Appl. 17, 64–75.

Litta, A.J., Mohanty, U.C., Kiran Prasad, S., Mohapatra, M., Tyagi, A., Sahu, S.C., 2012. Simulation of tornado over Orissa (India) on March 31, 2009, using WRF–NMM model. Nat. Hazards 61, 1219–1242. https://doi.org/10.1007/s11069-011-9979-1, 2012.

Mäkelä, A., Shrestha, R., Kark, R., 2014. Thunderstorm characteristics in Nepal during the pre- monsoon season 2012. Atmos. Res. 137, 91–99. https://doi.org/10.1016/j.atmosres.2013.09.012.

Mallapaty, S., 2019. Nepali scientists record country's first tornado. Nature. https://doi.org/10.1038/d41586-019-01159-w online.

Moller, A.R., Doswell III, C.A., Foster, M.P., Woodall, G.R., 1994. The operational recognition of supercell thunderstorm environments and storm structures. Weather Forecast. 9 (3), 327–347.

Monteverdi, J.P., Doswell III, C.A., Lipari, G.S., 2003. Shear parameter thresholds for forecasting tornadic thunderstorms in north-ern and central California. Weather Forecast. 18, 357–370.

Nakanishi, M., Niino, H., 2009. Development of an improved turbulence closure model for the atmospheric boundary layer. J. Meteor. Soc. Jpn. 87, 895–912. https://doi.org/10.2151/jmsj.87.895.

NAM. Technical report: National centers for environmental prediction environmental modeling center. Accessed online April 2021. https://www.emc.ncep.noaa.gov/mmb/mmbpll/misc/NAM_2017.pdf.

Peterson, P.E., Mehta, K.C., 1981. Climatology of tornadoes of India and Bangladesh. Arch. Met. Geoph. Biocl., Ser. B 29, 345–356. https://doi.org/10.1007/BF02263310.

Report on Bara Parsa Tornado, 2019. Government of Nepal Department of Hydrology and Meteorology. Accessed online. http://www.smallearth.org.np/wp- content/uploads/2019/04/Report-on-Bara-Parsa-Tornado.pdf.

Rosoff, Y.N., Hindman, E.E., 2002. Mt. Everest, 10 May 1996: study of a high elevation thunderstorm. In: 10th Conf. on Mountain Meteorology, vols. 17–21. American Meteorological Society, Park City, USA, 6.

Skamarock, W.C., Klemp, J.B., Dudhia, J., Gill, D.O., Barker, D., Duda, M.G., Huang, X.-Y., Wang, W., Powers, J.G., 2008. A Description of the Advanced Research WRF Version 3 (No. NCAR/TN-475+STR). University Corporation for Atmospheric Research. https://doi.org/10.5065/D68S4MVH.

Soriano, C, Jorba, O, Baldasano, J.M., 2004. One-Way Nesting Versus Two-Way Nesting: Does It Really Make a Difference? In: Borrego, C, Schayes, G (Eds.), Air Pollution Modeling and Its Application, XV. Springer, Boston, MA, pp. 177–185.

Stensrud, D.J., Cortinas Jr., J.V., Brooks, H.E., 1997. Discriminating between tornadic and nontornadic thunderstorms using mesoscale model output. Weather Forecast. 12 (3), 613–632.

Tewari, M., Chen, F., Wang, W., Dudhia, J., LeMone, M.A., Mitchell, K., Ek, M., Gayno, G., Wegiel, J., Cuenca, R.H., 2004. Implementation and verification of the unified NOAH land surface model in the WRF model. In: 20th Conference on Weather Analysis and Forecasting/16th Conference on Numerical Weather Prediction, pp. 11–15.

Thompson, R.L., Edwards, R., Hart, J.A., Elmore, K.L., Markowski, P., 2003. Close proximity soundings within supercell environments obtained from the Rapid Update Cycle. Weather Forecast. 18, 1243–1261.
Weisman, M.L., Klemp, J.B., 1982. The dependence of numerically simulated convective storms on vertical wind shear and buoyancy. Mon. Weather Rev. 110, 504–520.
WSEC, 2004. A recommendation for an ENHANCED FUJITA SCALE (EF-Scale). Wind Science and Engineering Center. Texas Tech University (June) Available at: https://www.spc.noaa.gov/faq/tornado/ef-ttu.pdf. (Accessed 25 January 2021).